Contributions of Wind Forcing and Surface Heating to Interannual Sea Level Variations in the Atlantic Ocean

CÉCILE CABANES, THIERRY HUCK, AND ALAIN COLIN DE VERDIÈRE

Laboratoire de Physique des Océans, Brest, France

(Manuscript received 20 July 2005, in final form 24 January 2006)

ABSTRACT

Interannual sea surface height variations in the Atlantic Ocean are examined from 10 years of high-precision altimeter data in light of simple mechanisms that describe the ocean response to atmospheric forcing: 1) local steric changes due to surface buoyancy forcing and a local response to wind stress via Ekman pumping and 2) baroclinic and barotropic oceanic adjustment via propagating Rossby waves and quasi-steady Sverdrup balance, respectively. The relevance of these simple mechanisms in explaining interannual sea level variability in the whole Atlantic Ocean is investigated. It is shown that, in various regions, a large part of the interannual sea level variability is related to local response to heat flux changes (more than 50% in the eastern North Atlantic). Except in a few places, a local response to wind stress forcing is less successful in explaining sea surface height observations. In this case, it is necessary to consider large-scale oceanic adjustments: the first baroclinic mode forced by wind stress explains about 70% of interannual sea level variations in the latitude band 18°–20°N. A quasi-steady barotropic Sverdrup response is observed between 40° and 50°N.

1. Introduction

Apart from responses to tidal and atmospheric pressure forcing, local sea surface height (SSH) variability in the open ocean bears the signature of change of many forcing and processes: buoyancy fluxes, wind stress, and mass fluxes at the air–sea interface, changing ocean water properties by advection of heat and salt, and baroclinic/barotropic instabilities (linked to horizontal and vertical shear), and sea ice melting/freezing. This results in local volume and mass changes that both contribute to SSH anomalies measured by satellite altimetry. A number of studies have been devoted to determine the importance of the various forcings in explaining the sea surface height variability. Because they depend on the period and latitude they contribute differently. Using numerical simulations, Fukumori et al. (1998) show that the large-scale and high-frequency sea level variability (period shorter than 100 days) is mainly wind-driven and that the ocean adjusts via propagating barotropic Rossby waves. On seasonal time scales, Gill and Niller (1973) show the importance of heat fluxes in midlatitudes via the steric response of the mixed layer, whereas Ferry et al. (2000) point out the role of advection in the western subtropical gyre. In the Pacific Ocean, Vivier et al. (1999) confirm the predominance of heat fluxes in midlatitudes and show the importance of propagating structures (Rossby and equatorial Kelvin waves) equatorward of 20°, while a topographic time-varying Sverdrup balance is proposed in the subpolar gyre. Other studies based on the comparison of XBT/CTD sections with altimetry have also shown that seasonal SSH anomalies are mainly related to density changes, even if barotropic variations are observed and linked to the time-varying barotropic Sverdrup balance of wind stress, for example, Mestas-Nuñez et al. (1992) in the South Pacific and Stammer (1997) in the North Pacific. On interannual time scales, there is less observational evidence of a time-varying barotropic Sverdrup balance [for an example along repeated World Ocean Circulation Experiment (WOCE) sections in the South Pacific subtropical gyre, see McCarthy et al. (2000)]. Decomposing the wind-driven response into barotropic and baroclinic components, Qiu (2002) shows that, after removing local steric changes induced by heat fluxes, the wind-forced first baroclinic Rossby wave is adequate to explain large-scale interannual sea

Corresponding author address: Cecile Cabanes, Jet Propulsion Laboratory, M/S 300-323, 4800 Oak Grove Dr., Pasadena, CA 91109.
E-mail: ccabanes@pacific.jpl.nasa.gov

level variability in the North Pacific. Other studies address the question of the role of eastern-boundary-forced baroclinic Rossby waves, in the North Pacific (Fu and Qiu 2002) and southeast Pacific (Vega et al. 2003). The influence of that boundary appears to be limited to no more than 1000–2000 km at midlatitudes. On decadal time scales, baroclinic Rossby waves forced by wind stress appear to be sufficient to explain the sea surface height variability at the Bermuda tide gauge (Sturges and Hong 1995). Moreover, the shape and level of low-frequency sea level variability in extratropical oceans are well predicted by a simple baroclinic Rossby wave model forced by stochastic wind stress (Frankignoul et al. 1997).

Recent studies based on altimeter-derived SSH have revealed interesting interannual variability in the Atlantic Ocean: Häkkinen (2001) shows that SSH in the North Atlantic exhibits a tripole pattern with an out-of-phase relationship between the Gulf Stream area and both the subpolar gyre and the Tropics. Moreover, complex EOF (CEOF) analysis (Fu 2004) makes clear a phase propagation from the subtropical region to the eastern end of the Gulf Stream extension. Other studies reveal large changes in the Gulf Stream and subpolar North Atlantic circulation during the 1990s: in particular, Flatau et al. (2003) document an intensified northeastward flow in the North Atlantic Current during 1992–95 relative to 1996–98. This is coincident with a shift in the North Atlantic Oscillation (NAO) index from positive to negative phase in winter 1995/96. A first step in exploring the underlying mechanisms of this interannual variability is to determine if simplified oceanic mechanisms, in response to atmospheric forcing, are relevant and sufficient to explain these observed changes. In particular, is baroclinic adjustment to wind forcing sufficient to explain interannual SSH variability in the midlatitudes as demonstrated by Sturges and Hong (1995) on decadal time scales? Are there regions where SSH changes are consistent with a time-dependent barotropic Sverdrup flow? Our goal is to investigate these questions using a simple dynamical framework. We investigate, in particular, 1) a local response to heat fluxes and wind forcing and 2) a large-scale adjustment to wind forcing under planetary geostrophic (PG) dynamics that includes both barotropic and baroclinic modes. Efficiency of the mechanisms in predicting sea level is assessed by computing a local hindcast skill.

2. Data processing

Sea surface height anomalies are obtained from the Archiving, Validation and Interpretation of Satellite Oceanographic data (AVISO)/Altimetry data center and correspond to a reprocessing of Ocean Topography Experiment (TOPEX)/Poseidon and European Remote Sensing Satellite (*ERS-1/2*) data. One map is provided every 7 days on a ⅓° grid. SSH maps were obtained using the mapping method detailed in Ducet et al. (2000). Instrumental and geophysical corrections (including the inverse barometer effect) are applied to the raw altimeter data. The nine full years available (1993–2001) are used in this study. To focus on interannual and large-scale variability, SSH are first averaged on a 1° grid with a 400-km Gaussian spatial filter. Then, SSH are monthly averaged, the seasonal cycle is removed, and then monthly anomalies are low-pass filtered with an 18-month Lanczos filter.

Global heat flux and precipitation data from the 40-yr European Centre for Medium-Range Weather Forecasts (ECMWF) Reanalysis (ERA-40) are used to compute the net surface heat flux Q and the difference between evaporation and precipitation (E–P). Monthly wind maps from the National Centers for Environmental Prediction (NCEP) (Kalnay et al. 1996) are also used to compute monthly wind stress curl since time coverage (1948–2001) is longer than for ECMWF wind. Wind stress curl is computed by using the bulk aerodynamic parameterization: $\boldsymbol{\tau} = \rho_a C_D U_a \mathbf{U}_a$, where $\boldsymbol{\tau}$ is the wind stress, $\rho_a = 1.25$ kg m^{-3} is the air density taken as a constant, C_D is the drag coefficient, and $\mathbf{U}_a$ is the wind velocity at 10 m. Here C_D is estimated using empirical coefficients (Hellerman and Rosenstein 1983). Wind stress curl was computed in polar spherical coordinates. Both monthly wind stress curl and monthly Q are then interpolated on the same $1° \times 1°$ grid as SSH.

3. Large-scale SSH interannual variability

Figure 1 shows the large-scale interannual variability (periods longer than 1.5 yr and spatial scales larger than 400 km) that is present in SSH. Largest variability is found in midlatitudes poleward of 25°–30°. Local maxima (3–5 cm) are found along the Gulf Stream path, in the Brazil–Malvinas confluence region and in the Agulhas Current retroflection region, whereas minima are found in the eastern North Atlantic and in the whole South Atlantic between 0°–20°S. Note that this large-scale interannual variability corresponds to about one-third of the total variability present in the 7-day ⅓° combined TOPEX/*ERS-1/2* product.

Empirical orthogonal function analysis is a suitable tool to give a space–time description of variability. The first two modes are shown on Fig. 2. They explain respectively 27% and 20% of the variability present in the 1.5-yr low-pass filtered data. The first mode (Fig. 2a) corresponds to a sea level rise between 1993 and 1999

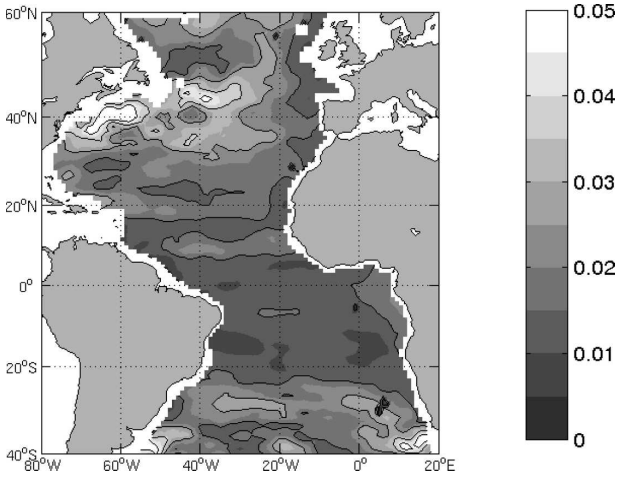

FIG. 1. Standard deviation of large-scale interannual sea surface height (m) based upon 1.5-yr low-pass-filtered time series.

that is observed in almost the whole Atlantic basin, even if the rise is stronger and thus more significant in the eastern North Atlantic and subpolar gyre. This strong sea level rise observed above 50°N has contributed to slowing down the circulation in this region during the 1990s in comparison with previous decades, as shown recently by Häkkinen and Rhines (2004).

The second mode (Fig. 2b) shows the familiar tripolelike oscillation in the North Atlantic. During the periods 1993–96 and 1999–2001 the region between 20° and 50°N corresponds to positive SSH anomalies embedded between negative anomalies. The reverse is observed during the period 1996–99. Changes from a phase of the tripolelike oscillation to another seem to be linked with the winter North Atlantic Oscillation index shifts in winters 1995/96 and 2001/02. Sea level rise observed in almost the whole basin during this pe-

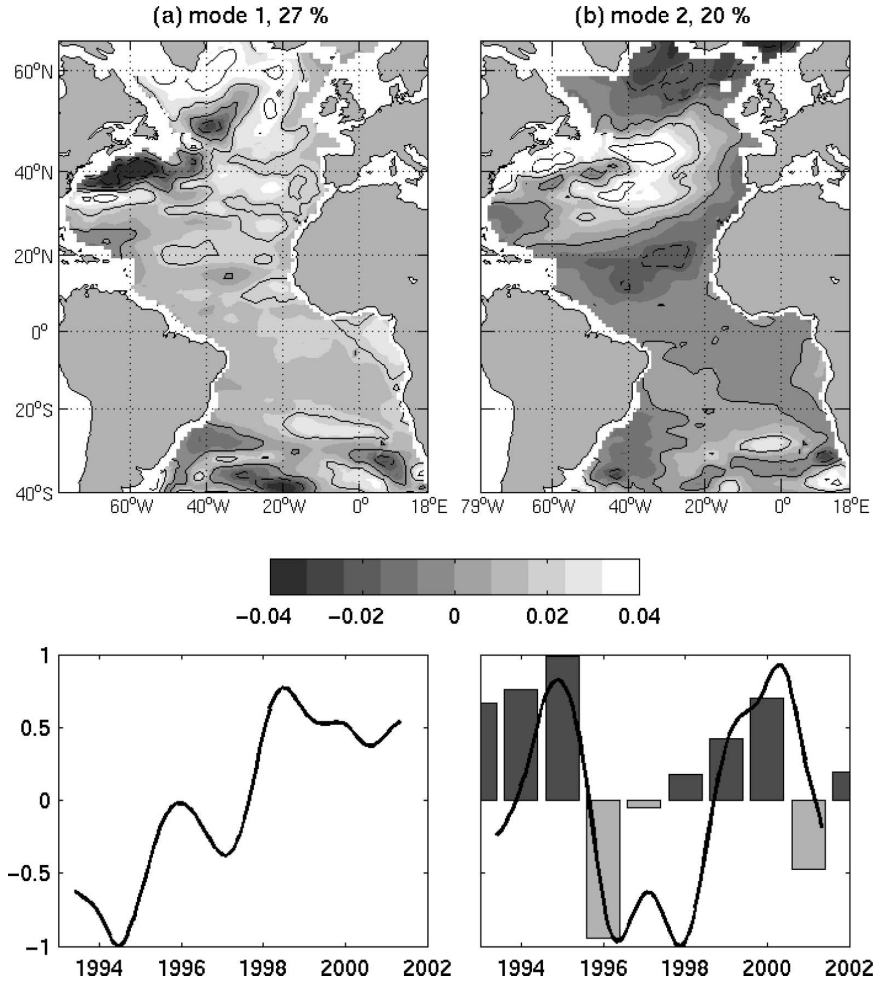

FIG. 2. Empirical orthogonal function analysis of sea surface height. (top) The spatial structure of (a) mode 1 and (b) mode 2. Units are meters and contours every 0.02 m. (bottom) Corresponding normalized temporal variations. Winter NAO index (available online at ftp://ftp.cru.uea.ac.uk/data) is superimposed (histogram) on the second-mode temporal variations.

riod is outside the scope of the present study, and we have removed the linear trend computed between 1993 and 2002 in the subsequent analyses.

4. Local response to atmospheric forcing

a. Diabatic steric height changes and Ekman pumping

Varying heat and freshwater surface fluxes produce local density changes in the upper ocean layers. Assuming no mass variations, these density changes result in diabatic steric height changes, which can be written as

$$\partial_t \eta_s = \frac{\alpha}{\rho_0 c_p}[Q(t) - \overline{Q(t)}] - \beta S_a(t)[E\text{–}P(t) - \overline{E\text{–}P(t)}], \tag{1}$$

where ρ_0 is the reference density, c_p is the specific heat of seawater, α and β are the coefficients of thermal and haline expansion, $Q(t)$ is the net surface heat flux, and E–P is the freshwater flux; $Q(t)$ and E–$P(t)$ are monthly time series from the ECMWF reanalysis, and overbars denote the temporal average. The averages $\overline{Q(t)}$ and $\overline{E\text{–}P(t)}$ are removed since sea level trends are outside our focus. Here α and β fields are estimated from the monthly climatologies of temperature and salinity from the *World Ocean Atlas 2001* (*WOA01*; Stephens et al. 2001; Boyer et al. 2001) averaged over mixed layer depth (the latter is computed using a potential density criteria of 0.125 from the surface value). Throughout the basin ρ_0 and c_p are taken constant ($\rho_0 = 1000$ kg m^{-3} and $c_p = 3960$ J kg^{-1} K^{-1}).

Density fields can also be affected by varying wind forcing through vertical Ekman pumping of the mean thermocline. In a stratified ocean, local density changes due to vertical advection w' can be written as

$$\partial_t \rho = \rho_0 g^{-1} w' N^2, \tag{2}$$

with N being the Brunt–Väisälä frequency.

To estimate this contribution without calculating the dynamic response, Gill and Niller (1973) assumed that w' varied linearly from $w' = w_{\mathrm{Ek}}$ at the top to $w' = 0$ at the ocean flat bottom and deduced steric changes by vertically integrating the density anomalies:

$$\partial_t \eta_{\mathrm{Ek}} = -\mathcal{A}\,\mathrm{curl}\left(\frac{\boldsymbol{\tau}}{\rho_0 f}\right), \tag{3}$$

where

$$\mathcal{A} = g^{-1}\int_{-H}^{0} N^2(1 + z/H)\,dz. \tag{4}$$

The zonally averaged standard deviation of the two forcing terms that appear in (1) and (3), related to wind stress and local buoyancy fluxes respectively, are compared in Fig. 3 as a function of latitude for interannual time scales (i.e., the 1.5-yr low-pass filter is applied). Wind stress forcing is stronger at low latitudes because of the decreasing Coriolis parameter f. Other local maxima are reached at various latitudes, mainly around 20°S and 20°N and around 45°N. Interannual heat flux forcing is in the same range of magnitude as wind forcing, smaller equatorward of 30° and larger poleward. In the North Atlantic, the heat flux forcing has maxima of interannual variability around 18°–20° and 40°N. The variability related to E–P is smaller by an order of magnitude. Even if this term can be important locally, we neglected it in the following.

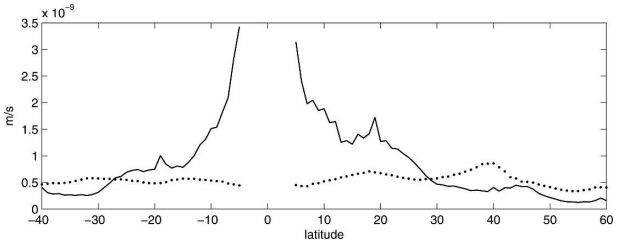

FIG. 3. Zonal mean standard deviation (m s^{-1}) for $\mathcal{A}\,\mathrm{curl}(\boldsymbol{\tau}/\rho_0 f)$ (solid line) and $\alpha Q/(\rho_0 c_p)$ (dotted line).

b. Comparison with altimetry

Figure 4 shows the skill S for diabatic steric changes and local Ekman pumping in accounting for the variance of TOPEX/Poseidon sea level anomaly (SLA). This skill is defined by

$$S = 1 - \frac{\langle(\eta_o - \eta_p)^2\rangle}{\langle(\eta_o)^2\rangle}, \tag{5}$$

where η_o and η_p are, respectively, the observed and predicted sea level anomalies, and angle brackets denote time averaging. Skill ranges between $-\infty$ and 1. High values for skill ($S \to 1$) indicate that observed and predicted SSH are both well correlated and of the same magnitude. Negative values denote low or negative correlations and/or larger magnitude for predicted SSH. The skill is given as a percentage of the observed variance depicted in Fig. 1.

Diabatic steric changes resulting from local heat flux forcing correctly reproduce interannual sea level variations in various locations, for instance in the midlatitudes of the northeastern basin where about 50% of variance is explained (Fig. 4a). The comparison is less successful in western boundary current regions and equatorward of 30°.

On the other hand, local Ekman pumping fails to reproduce interannual altimetrically derived sea level

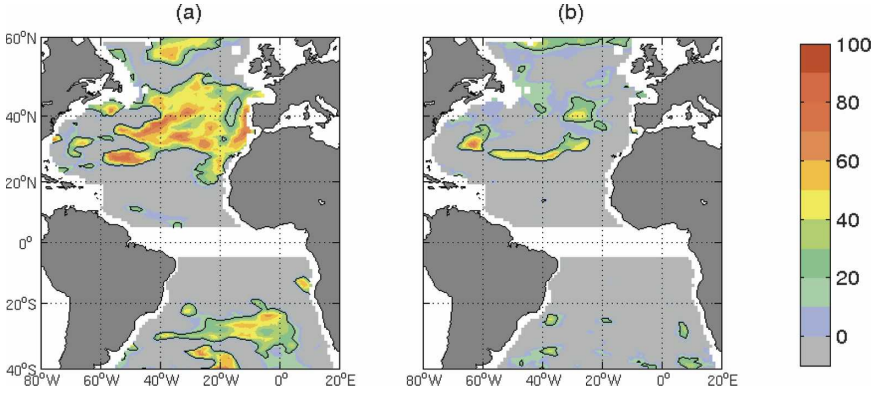

FIG. 4. Skill (%) of (a) local steric height variations and (b) Ekman pumping in accounting for the interannual variance of altimetric sea surface height. Contours indicate a skill of 20%.

variations (Fig. 4b). Although local changes in surface heat flux show some skill in explaining the sea level variability, we expect that the lack of ocean dynamics in the derivation of (3) is the cause for the poor contribution of wind forcing. This is explored in the next section.

5. Large-scale oceanic adjustment to atmospheric forcing: Formulation with planetary geostrophic dynamics

For interannual time scales long relative to barotropic Rossby wave propagation across the basin and spatial scales large relative to the Rossby radius of deformation, planetary geostrophic (PG) dynamics are appropriate. This allows one to keep the full variations of f with latitude and to calculate the response on the sphere (as compared with quasigeostrophic dynamics, which require a β plane). A simple linear long-wave PG model is used to estimate the response of the ocean to wind stress. The long-wave assumption excludes the equatorial region as dispersion effects become important (Chang and Philander 1989). We neglect bottom topography and assume a rigid lid at the top. We also neglect advection by mean currents. Recent work (Colin de Verdière and Tailleux 2005) indicates that this reasonable assumption at low latitudes becomes increasingly difficult to defend at high latitudes, say beyond 35°. Consequently, the PG equations are written as

$$f\mathbf{k}\times\mathbf{u} = -\nabla\Pi + \frac{\boldsymbol{\tau}}{\rho_0 h}G(z), \tag{6}$$

where $\mathbf{k}$ is the vertical unit vector, and $\Pi = P/\rho_0$ the kinematic pressure. Here the wind forcing is introduced as a body force in the mixed layer of constant depth h through the function $G(z)$, which is 0 for $z < -h$ and 1 for $z > -h$.

Taking the curl of (6) and using the continuity equation gives

$$\beta v = f\partial_z w + \mathrm{curl}\left(\frac{\boldsymbol{\tau}}{\rho_0 h}\right)G(z), \tag{7}$$

where $\beta = 2\Omega a^{-1}\cos\theta$, with a being the earth radius and θ being the latitude.

a. Barotropic contribution to sea level

Consider first the determination of the depth-averaged flow $\mathbf{u}^+$, the barotropic mode. With a rigid lid at the surface and a flat bottom, the vertical integral of (7) yields the Sverdrup relation:

$$\beta v^+ = \mathrm{curl}\left(\frac{\boldsymbol{\tau}}{\rho_0 H}\right). \tag{8}$$

By inserting v^+ into the depth-averaged zonal momentum balance (6), the equation for the depth-averaged pressure Π^+ is obtained:

$$\beta\partial_x\Pi^+ = \frac{f^2}{H}\mathrm{curl}\left(\frac{\boldsymbol{\tau}}{\rho_0 f}\right), \tag{9}$$

where the derivation operator ∂_x is short for $(a\cos\theta)^{-1}\partial_\phi$, with ϕ being the longitude. Note that (9) is diagnostic because the rigid-lid boundary condition makes the speed of the barotropic Rossby waves infinite; hence the adjustment of the barotropic mode is instantaneous.

To obtain the barotropic-mode contribution to sea level $\eta^+ = \Pi^+/g$ from the wind forcing using (9), it is readily seen that a lateral boundary condition on Π^+ is required. This will be taken as usual at the eastern boundary ($x = x_e$) where the barotropic transport vanishes. However, the barotropic pressure needs not vanish since, at a meridional wall, (6) requires that

$$-\partial_y\Pi^+ + \frac{\tau_y}{\rho_0 H} = 0, \quad \text{at} \quad x = x_e, \tag{10}$$

where ∂_y is short for $a^{-1}\partial_\theta$.

This is a difficult condition to implement since (10) now couples the pressure at different latitudes. We have decided to ignore the barotropic forcing by the meridional wind at the eastern boundary, replacing the above boundary condition by $\Pi^+ = 0$ on the eastern side of the basin, hence focusing our attention solely on the effect of the interior wind forcing. The barotropic mode contribution to sea level η^+ is then simply

$$\eta^+(x,t) = \int_{x_e}^{x} \frac{f^2}{Hg\beta}\,\mathrm{curl}\left(\frac{\boldsymbol{\tau}}{\rho_0 f}\right) dx. \tag{11}$$

b. Baroclinic contributions to sea level

To obtain the equation for the baroclinic modes, we simply subtract (8) from (7):

$$\beta v^- = f\partial_z w + \mathrm{curl}\left(\frac{\boldsymbol{\tau}}{\rho_0 H}\right)K(z), \tag{12}$$

with $K(z) = (H/h)G(z) - 1$.

By expressing v^- as a function of the pressure Π^- from the baroclinic-mode version of (6), (12) becomes

$$\beta\partial_x\Pi^- = f^2\partial_z w + \frac{f^2}{H}\,\mathrm{curl}\left(\frac{\boldsymbol{\tau}}{\rho_0 f}\right)K(z). \tag{13}$$

Combining the hydrostatic and linearized density equations gives

$$\partial_{zt}\Pi^- + N^2 w = 0, \quad \text{at} \quad z \neq 0; \tag{14a}$$

$$\partial_{zt}\Pi^- = 0, \quad \text{at} \quad z = 0 \quad \text{and} \quad z = -H. \tag{14b}$$

If we eliminate w between (13) and (14a), a planetary geostrophic vorticity equation free from β-plane approximations is obtained with pressure as the dependant variable:

$$\partial_z\left(\frac{f^2}{N^2}\,\partial_{zt}\Pi^-\right) + \beta\partial_x\Pi^- = \frac{f^2}{H}\,\mathrm{curl}\left(\frac{\boldsymbol{\tau}}{\rho_0 f}\right)K(z); \tag{15a}$$

$$\partial_{zt}\Pi^- = 0, \quad \text{at} \quad z = 0 \quad \text{and} \quad z = -H. \tag{15b}$$

With a flat bottom, the vertical dependence is separable from the horizontal one, and the vertical baroclinic structure $F(z)$ satisfies

$$\partial_z\left(\frac{f^2}{N^2}\,\partial_z F\right) + \lambda^2 F = 0; \tag{16a}$$

$$\partial_z F = 0, \quad \text{at} \quad z = 0 \quad \text{and} \quad z = -H. \tag{16b}$$

The eigenvalue problem (16) is satisfied by an infinity of vertical modes $F_n(z)$ associated with eigenvalues λ_n. The modes are orthogonal and normalized such that $F_n(z)$ are dimensionless and verify

$$\frac{1}{H}\int_{-H}^{0} F_n(z)F_m(z)\,dz = \delta_{nm}. \tag{17}$$

The modes thus form a complete basis so that we can write the solution Π^- for the ocean interior as

$$\Pi^- = \sum_{n-1}^{\infty} p_n(x,y,t)F_n(z). \tag{18}$$

Then, Eq. (15a) is multiplied by $F_n(z)$ and integrated from top to bottom to obtain the amplitude p_n for each baroclinic mode:

$$\partial_t p_n + C_{rn}\partial_x p_n = -\frac{f^2}{\lambda_n^2 H}\,\mathrm{curl}\left(\frac{\boldsymbol{\tau}}{\rho_0 f}\right)H^{-1}\int_{-H}^{0} K(z)F_n(z)\,dz, \tag{19}$$

where $C_{rn} = -\beta/\lambda_n^2$ is the baroclinic Rossby wave phase speed.

Baroclinic-mode contribution to sea level $\eta_n^- = F_n(0)p_n/g$ can be obtained analytically by integrating (19) from the eastern boundary (x_e), along the Rossby wave characteristic in the (x, t) plane. Defining the coefficients $\mathcal{A}_n$ as

$$\mathcal{A}_n \equiv \frac{F_n(0)f^2}{gH\lambda_n^2}\,H^{-1}\int_{-H}^{0} K(z)F_n(z)\,dz, \tag{20}$$

the solution is written as

$$\eta_n^-(x,t) = \eta_n^-(x_e, t - t_e) - C_{rn}^{-1}\int_{x}^{x_e}\left[\mathcal{A}_n\,\mathrm{curl}\left(\frac{\boldsymbol{\tau}}{\rho_0 f}\right)\right](x', t - t_{x'})\,dx', \tag{21}$$

where $t_e = (x - x_e)/C_{rn}$ and $t_{x'} = (x - x')/C_{rn}$ are propagation times of the waves generated at the eastern boundary (first term in rhs) and by local atmospheric forcing east of the point x (second term in rhs), respectively.

The analytical solutions (11) and (21) of (19) are then numerically evaluated for each 1° latitude band separately between 40°S and 65°N in the Atlantic basin with the exclusion of the area 4°S–4°N. The corresponding zonal mean values for f, β, C_{rn}, H, and $\mathcal{A}_n$ are used. For the calculations presented in the next section, numerical integration starts in year 1948 with zero initial conditions. Then, the values predicted for our altimetric observation period (1993–2001) are thus independent of the initial conditions for mode 1 (2) up to latitude 50°N (35°N).

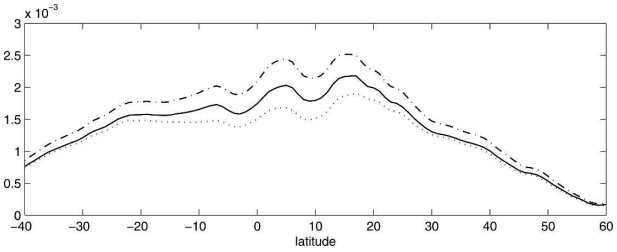

FIG. 5. Values of the coefficient $\mathcal{A}_1$ for $h = 100$ m (solid line), $h = 200$ m (dash–dotted line), and $h = 50$ m (dotted line) as a function of latitude.

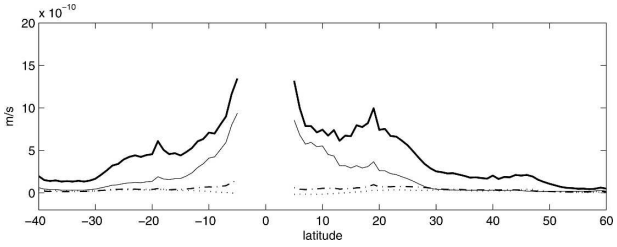

FIG. 6. Zonal mean standard deviation (m s^{-1}) for the forcing term in (19) $\{\mathcal{A}_n \mathrm{curl}[\boldsymbol{\tau}/(\rho_0 f)]\}$ projected onto mode 1 (thick solid line), mode 2 (thin solid line), mode 3 (dashed line), and the sum of all the other modes (dotted line).

c. Discussion

The coefficients $\mathcal{A}_n$ are easy to calculate knowing the vertical structure $F_n(z)$ and λ_n from (16) and mean annual hydrographic profiles (*WOA01*). However, this coefficient is also a function of the parameter h, the depth of the mixed layer that we chose quite arbitrarily to be 100 m. It is thus essential to first determine the uncertainties on $\mathcal{A}_n$ values related to the choice of h. Figure 5 compares $\mathcal{A}_1$ for various values of h as a function of latitude. The ocean response to wind forcing decreases with increasing h. Differences are larger at low latitudes, reaching 20% at 5°–10° when $\mathcal{A}_1$ is computed with $h = 200$ m instead of $h = 100$ m, for example.

We now examine the wind stress forcing of each mode. The wind stress forcing projects onto different modes, and the resulting standard deviations of the interannual time series are plotted in Fig. 6, showing the importance of the first two baroclinic modes. For that reason only these two modes are discussed in what follows.

6. Comparison of computed sea level with observed sea surface height

In this section, we examine whether the physical processes described above account for the variance of altimetric sea surface height. The skill S, defined in (5), is used to compare quantitatively observed and predicted SSH anomalies.

a. Baroclinic modes forced by wind

Figure 7a shows the contribution of the first baroclinic modes forced by the wind stress. It explains a significant fraction of the interannual variability observed by altimetry in two regions: the 15°–20°N zonal band (between 40% and 90% of variance) and the 5°–10°S zonal band (between 20% and 50% of variance). Note that in these two regions, the baroclinic wave model gives better results than the local Ekman pumping response (see Fig. 4). At higher latitudes, several small regions where skills range between 20% and 50% are also observed.

Before going further, it should be reminded that the linear baroclinic wave model is run here with theoretical Rossby wave phase speeds (16). However, it is well known that observed westward phase speeds of propagating structures detected in altimetry are faster than expected from classical linear theory (Chelton and Schlax 1996; Killworth et al. 1997). The physical mechanisms responsible for the differences remain to be clearly identified among a number of possibilities: forcing, background currents, nonuniform bottom topography, and so on. However, extending the standard theory, Killworth et al. (1997) have shown that vertically sheared mean currents are able to increase phase speeds, which reduces differences with observed phase speeds. Colin de Verdière and Tailleux (2005) have shown, however, that this accelerating effect is restricted to latitudes between 35° and 45° in the case of eastward surface currents. To take into account mean currents, several studies ran standard linear baroclinic wave models with observed speeds instead of theoretical ones, yielding a better agreement between the first baroclinic mode forced by wind stress and altimetric SSH in the Pacific Ocean (Fu and Qiu 2002; Qiu 2003). Similarly, as a test, we have added a speed c' to the standard first-baroclinic-mode phase speed C_{r1} in such a way that $C_{r1} + c'$ matches C_{obs}, where C_{obs} is the observed speed of propagating structures detected in altimetric SSH. Equatorward of 25°, skills obtained in case of wind stress forcing alone are very similar to those obtained previously (when theoretical phase speed are used; see Fig. 7a). This is not surprising because in these regions observed and theoretical speeds are rather close. Larger skills are found poleward in two regions: the eastern North Atlantic (eastward of 40°W and between 30° and 45°N) and in the South Atlantic (35°–40°S).

The second baroclinic mode (Fig. 7b) does not explain significantly the observed sea surface height ex-

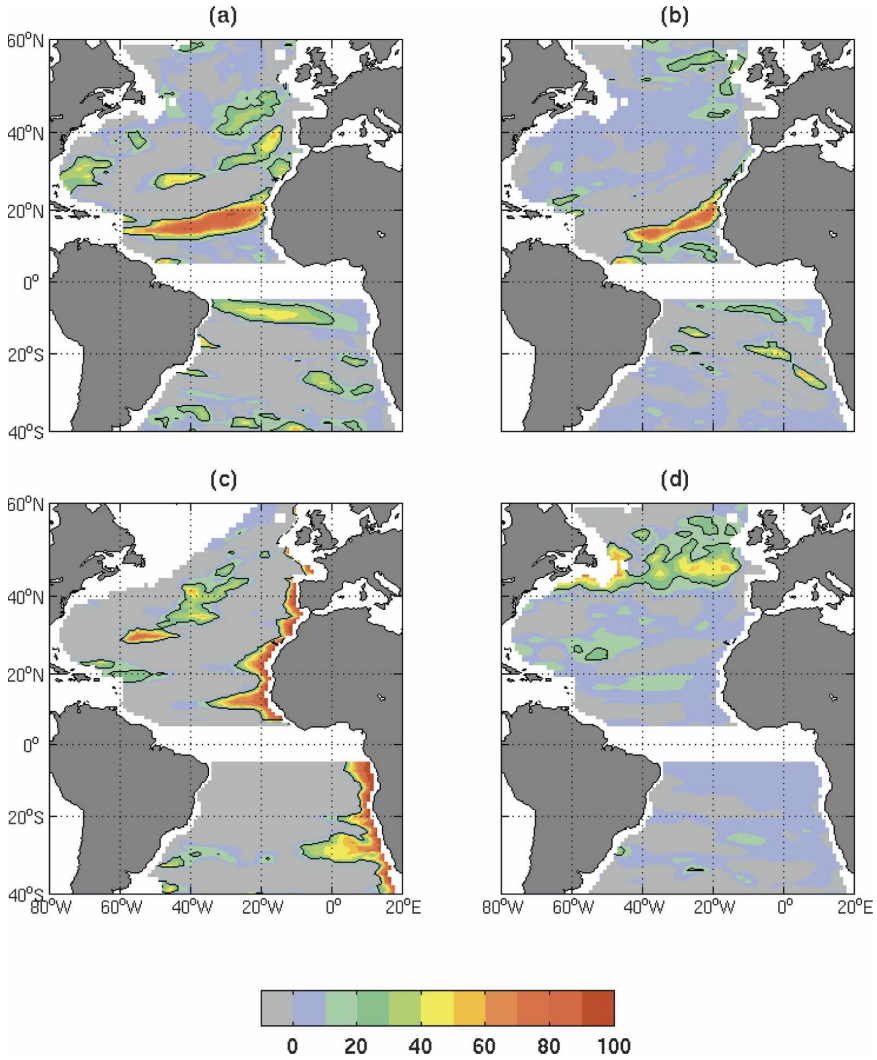

FIG. 7. As Fig. 4 but with (a) wind-forced first baroclinic mode, (b) wind-forced second baroclinic mode, (c) eastern-boundary-generated Rossby waves (first mode), and (d) time-varying Sverdrup balance.

cept in the eastern Atlantic, between 10° and 20°N. Note, moreover, that adding the two first modes generally does not improve (or reduce) skills for observed SSH.

b. *First baroclinic mode forced by the eastern boundary*

Figure 7c is the contribution of boundary-driven Rossby waves to sea level interannual variability, which corresponds to the first term in (21). Notice that a Rossby wave forced at the eastern side crosses the Atlantic basin in about 2 years at 20°N (or S), whereas it takes about 15 years at 40°N and more than 45 years at 55°N. We have assumed that the altimetric observations in the 1° cell closest to the coast project onto the first baroclinic mode and thus correspond to $\eta_1(x_e, t)$. We have removed frequencies that are not able to propagate away from the boundary (Clarke and Shi 1991), following the method used in the Pacific basin by Fu and Qiu (2002). Results in the Atlantic are quite similar: the contribution of boundary-driven Rossby waves appears to be significant only in the vicinity of the east coast, apart for some latitudes (around 30°S, 10° and 22°N) where a contribution larger than 80% extends between 1000 or 2000 km to the west. Notice that this does not mean the waves themselves are trapped into that region.

c. *Barotropic mode*

Figure 7d is the contribution of barotropic mode to sea surface height interannual variations given by (11). This contribution is mostly weak, except in the 40°–

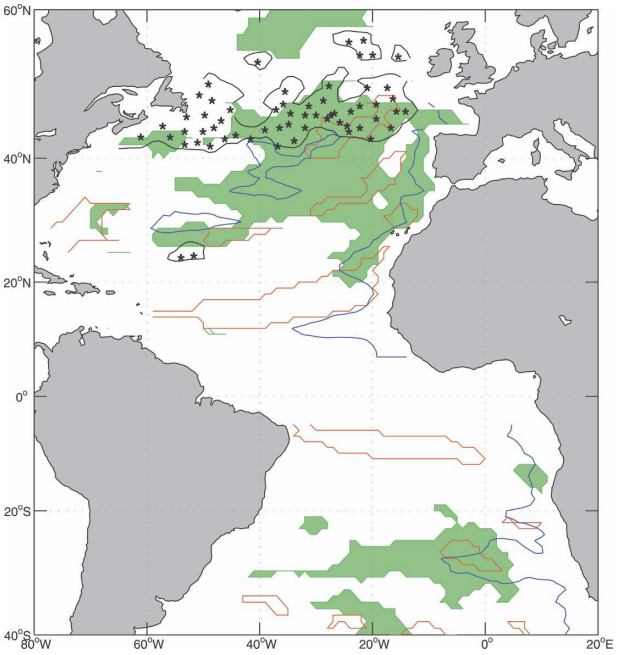

FIG. 8. Part of interannual SSH variability that can be explained by simple mechanisms describing sea level response to atmospheric forcing with skill >20%: 1) local steric changes (green patch), 2) first baroclinic mode (red contour) forced by interior wind stress, 3) first baroclinic mode (blue contour) forced by eastern boundary, and 4) barotropic mode (black contour filled with black stars).

50°N latitude band, where it explains between 20% and 50% of the observed variance. If we look at Fig. 3, its appears that interannual variability of Ekman pumping is relatively important, about 0.4×10^{-6} m s^{-1} in zonal average. This is also consistent with the large zonal coherency of Ekman pumping interannual changes of about 1300 km zonally averaged, or one-third of the zonal basin size at these latitudes. The decorrelation length is computed as the minimum distance at which correlations decrease to values lower than 0.5, as in Capotondi et al. (2003). This coherency could justify why zonally integrating Ekman pumping anomalies give rise to sufficiently large η^+ changes that explain a significant part of observed sea surface height variability in this region.

7. Discussion and conclusions

Wind stress and heat flux forcing from the reanalyses center were used to investigate the ability of simple oceanic mechanisms in reproducing interannual SSH variations observed by altimetry from the TOPEX/Poseidon and *ERS-1/2* satellites in the whole Atlantic basin (40°S–60°N). Figure 8 summarizes results of sections 4 and 6. As expected, the local response to heat

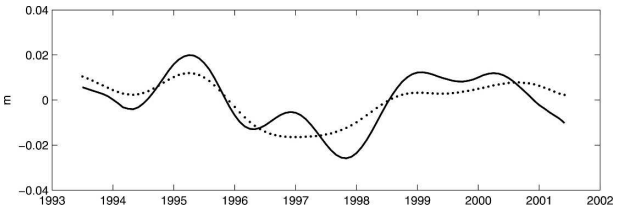

FIG. 9. Sea surface height variations averaged between 30° and 50°N in the North Atlantic basin from altimetry (solid) and from local steric response to heat fluxes (dashed).

flux changes is able to explain a large part of the sea level interannual variability in middle and high latitudes, away from boundary currents. For example, diabatic steric changes explain more than 60% of interannual SSH variations averaged between 30° and 50°N in the North Atlantic basin and thus positive sea level anomalies observed in this region in 1994–96 and 1999–2001 (see Fig. 9). It appears that the remaining SSH interannual variations, after correcting from local steric changes induced by heat fluxes (see Fig. 10), are rather well explained by the large-scale adjustment to wind stress (barotropic mode plus first and second baroclinic modes) in two locations, 40°–50° and 15°–20°N. Remaining SSH averaged between 40° and 50°N is explained for about 60% by the large-scale adjustment to wind forcing (Fig. 11a). The barotropic Sverdrup balance contributes for the most part (52%) for the short time scales (not shown): it constitutes a fast response to the wind stress forcing (the correlation between the time-dependent Sverdrup flow, and the NAO is 0.7 at 0 lag, significant at 95%). Between 15° and 20°N the re-

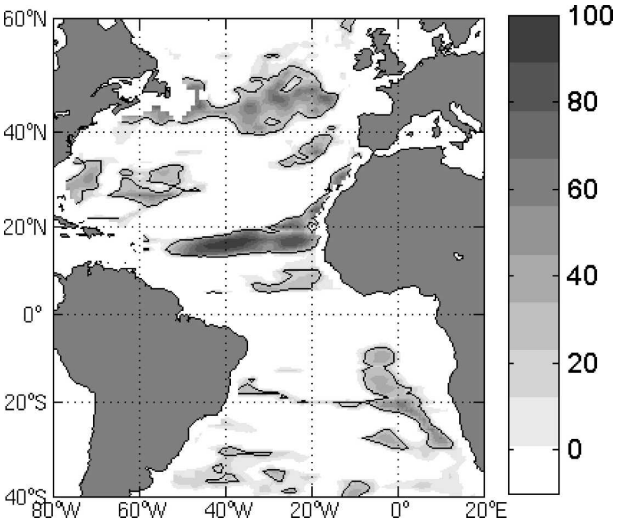

FIG. 10. Skill (%) of large-scale adjustment to wind stress (barotropic and the two first baroclinic modes) in accounting for the interannual variance of altimetric sea surface height corrected from local steric changes. Contours indicate a skill of 20%.

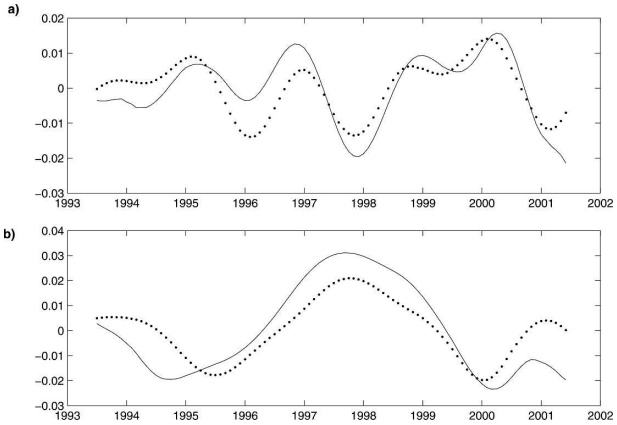

FIG. 11. Sea surface height variations in the North Atlantic basin averaged between (a) 40° and 50°N and (b) 15° and 20°N. Solid line corresponds to remaining SSH after correcting from local steric changes, and dotted line corresponds to the large-scale adjustment to wind stress, i.e., barotropic plus the two first baroclinic modes.

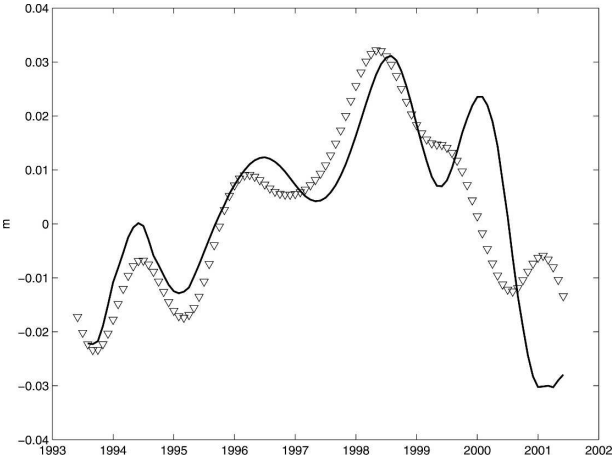

FIG. 12. Sea surface height observed (solid line) from altimetry near Bermuda (32°N, 64°W) and predicted (triangle) from the first baroclinic mode forced by wind plus the local steric response to heat fluxes.

maining SSH is explained by the large-scale adjustment to wind forcing (66%; Fig. 11b) and mainly by the first baroclinic mode (60%). Note that our simple linear model is insufficient to explain the propagation, highlighted by the analysis of Fu (2004), that occurs between 20°–30°N in the subtropics. Adjusting the Rossby phase speed to those observed in our linear model does not improve the results. Mechanisms underlying SSH propagation between 20° and 30°N remain to be determined.

At interannual time scales we are able to explain about 70% of the variability near Bermuda (32°N, 64°W), with 40% from propagating Rossby waves forced by wind and 30% by local steric response to heat flux changes (Fig. 12): the two time series are not correlated at this time scale and the skills are thus additive. These results are somewhat different from those of Sturges and Hong (1995) who found that, at decadal time scales, sea level at Bermuda could be explained solely by propagating wind-forced Rossby waves. Note that, unlike these authors, we have chosen not to include the varying phase speed with longitude. This might increase the skill for wind-driven Rossby waves but at the expense of a model difficult to rationalize.

Considering both local steric changes induced by heat fluxes and large-scale adjustment to wind forcing is, however, far insufficient to explain the interannual sea level variability in many regions of the Atlantic Ocean: among them, western boundary regions, which are known for strong eddy kinetic energy. To evaluate the role of the internal variability of the ocean at interannual time scales, which is not directly related to air–sea forcings, we used outputs from the eddy-resolving ocean model "CLIPPER" at ⅙° (Treguier et al. 2001). In this aim, two runs are examined: "the annual cycle run" (i.e., ATL6-V5) and the "interannual run" (i.e., ATL6–26). The annual cycle run has no interannual variability in the forcing (the same mean-annual-cycle forcing is applied repeatedly during a period of 20 yr). Figure 13a shows the standard deviation of sea surface height from the 20-yr annual cycle run after all spatial scales smaller than $R = 400$ km and time scales shorter than 1.5 yr had been filtered. The residual variability present in Fig. 13a is thus attributable to the internal variability. The interannual run is forced with the actual daily fields from ECMWF, covering the period 1993–2002. It shows clearly that a large part of variability in the Gulf Stream and North Atlantic Current region, as well as in the Agulhas Current retroflection area, can be generated by other internal processes. This could well explain the deficiency of our simple models to reproduce sea surface height variability in these regions.

The aim of the present study was to investigate the relevance of simple mechanisms in explaining interannual sea level variability in the whole Atlantic Ocean. A local response to heat flux changes explain SSH variations in various regions of the Atlantic basin, especially outside of boundary current regions. In these regions, the advection by anomalous or mean geostrophic currents can largely contribute to interranual variations of the upper-layer heat content (Dong and Kelly 2004). We have shown that the remaining SSH after correcting from local steric changes was relatively well explained by the quasi-steady barotropic Sverdup balance between 40° and 50°N. The large-scale adjustment to wind forcing via the propagation of Rossby waves agrees best with the remaining SSH in the 15°–

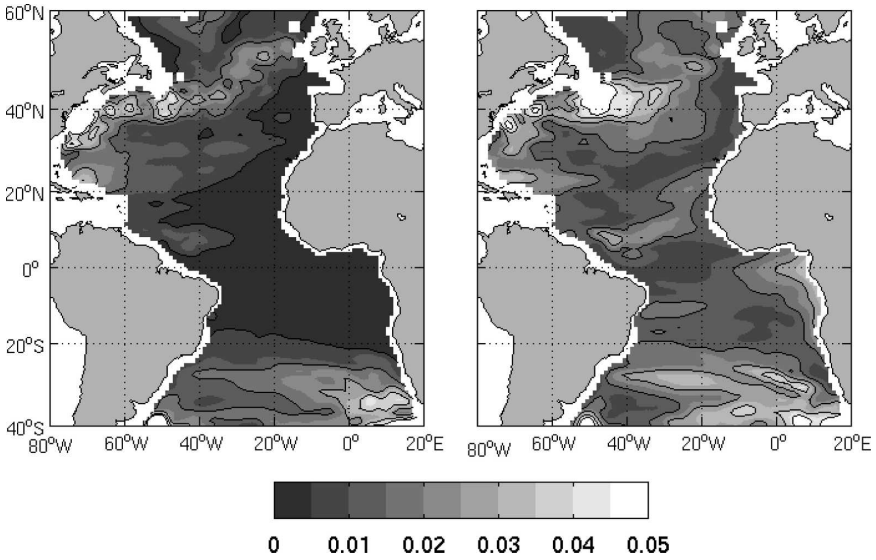

FIG. 13. Standard deviation of large-scale interannual sea surface height (m) from the CLIPPER model, based upon 1.5-yr low-pass-filtered time series with linear trend removed: (a) the ATL6-V5 simulation with climatological atmospheric forcing; (b) the ATL6-26 simulation with interannual atmospheric forcing.

20°N region. Using CLIPPER simulations we have demonstrated that the internal variability of the ocean can explain an important part of the interannual and large-scale variability present in the altimetric SSH, whose mechanisms include various instabilities and/or topographic effects. Clearly, high-resolution studies are necessary to identify and quantify the respective contribution of atmospheric forcing (wind and buyoancy) and internal variability to the interannual SSH changes.

Acknowledgments. Anne Marie Treguier and Jean-Marc Molines provided us with the CLIPPER simulations. ECMWF ERA-40 data used in this study have been obtained from the ECMWF data server. NCEP reanalyses data are provided by the NOAA–CIRES Climate Diagnostics Center, Boulder, Colorado, on their Web site (http://www.cdc.noaa.gov/). Cecile Cabanes is funded through an IFREMER postdoctoral fellowship.

REFERENCES

Boyer, T. P., C. Stephens, J. I. Antonov, M. E. Conkright, R. A. Locarnini, T. D. O'Brien, and H. E. Garcia, 2001: *Salinity*. Vol. 2, *World Ocean Atlas 2001,* NOAA Atlas NESDIS 50, 165 pp.

Capotondi, A., M. A. Alexander, and C. Deser, 2003: Why are there Rossby wave maxima in the Pacific at 10°S and 13°N? *J. Phys. Oceanogr.,* **33,** 1549–1563.

Chang, P., and S. G. H. Philander, 1989: Rossby wave packets in baroclinic mean currents. *Deep-Sea Res.,* **36A,** 17–37.

Chelton, D. B., and M. G. Schlax, 1996: Global observation of oceanic Rossby waves. *Science,* **272,** 234–238.

Clarke, A. J., and C. Shi, 1991: Critical frequencies at ocean boundaries. *J. Geophys. Res.,* **96,** 10 731–10 738.

Colin de Verdière, A., and R. Tailleux, 2005: The interaction of a baroclinic mean flow with long Rossby waves. *J. Phys. Oceanogr.,* **35,** 865–879.

Dong, S., and K. A. Kelly, 2004: Heat budget in the Gulf Stream region: The importance of heat storage and advection. *J. Phys. Oceanogr.,* **34,** 1214–1231.

Ducet, N., P. Y. Le Traon, and G. Reverdin, 2000: Global high resolution mapping of ocean circulation from TOPEX/Poseidon and *ERS-1/2*. *J. Geophys. Res.,* **105,** 19 477–19 498.

Ferry, N., G. Reverdin, and A. Oschlies, 2000: Seasonal sea surface height variability in the North Atlantic Ocean. *J. Geophys. Res.,* **105,** 6307–6326.

Flatau, M. K., L. Talley, and P. P. Niiler, 2003: The North Atlantic Oscillation, surface current velocities, and SST changes in the subpolar North Atlantic. *J. Climate,* **16,** 2355–2369.

Frankignoul, C., P. Müller, and E. Zorita, 1997: A simple model of the decadal response of the ocean to stochastic wind forcing. *J. Phys. Oceanogr.,* **27,** 1533–1546.

Fu, L. L., 2004: The interannual variability of the North Atlantic Ocean revealed by combined data from TOPEX/Poseidon and Jason altimetric measurements. *Geophys. Res. Lett.,* **31,** L23303, doi:10.1029/2004GL021200.

——, and B. Qiu, 2002: Low-frequency variability of the North Pacific Ocean: The roles of boundary- and wind-driven baroclinic Rossby waves. *J. Geophys. Res.,* **107,** 3220, doi:10.1029/2001JC001131.

Fukumori, I., R. Raghunath, and L. Fu, 1998: Nature of global large-scale sea level variability in relation to atmospheric forcing: A modeling study. *J. Geophys. Res.,* **103,** 5493–5512.

Gill, A. E., and P. P. Niller, 1973: The theory of the seasonal variability in the ocean. *Deep-Sea Res.,* **20,** 141–177.

Häkkinen, S., 2001: Variability in sea surface height: A qualitative

measure for the meridional overturning in the North Atlantic. *J. Geophys. Res.,* **106,** 13 837–13 848.

——, and P. B. Rhines, 2004: Decline of subpolar North Atlantic circulation during the 1990s. *Science,* **304,** 555–559.

Hellerman, S., and M. Rosenstein, 1983: Normal monthly wind stress over the World Ocean with error estimates. *J. Phys. Oceanogr.,* **13,** 1093–1104.

Kalnay, E., and Coauthors, 1996: The NCEP/NCAR 40-Year Reanalysis Project. *Bull. Amer. Meteor. Soc.,* **77,** 437–471.

Killworth, P. D., D. B. Chelton, and R. A. De Szoeke, 1997: The speed of observed and theoretical long extratropical planetary waves. *J. Phys. Oceanogr.,* **27,** 1946–1966.

McCarthy, M., L. Talley, and D. Roemmich, 2000: Seasonal to interannual variability from expendable bathythermograph and TOPEX/Poseidon altimeter data in the South Pacific subtropical gyre. *J. Geophys. Res.,* **105,** 19 535–19 550.

Mestas-Nuñez, A., D. Chelton, and R. DeSzoeke, 1992: Evidence of time-dependent Sverdrup circulation in the South Pacific from *Seasat* scatterometer and altimeter. *J. Phys. Oceanogr.,* **22,** 934–943.

Qiu, B., 2002: Large-scale variability in the midlatitude subtropical and subpolar North Pacific Ocean: Observations and causes. *J. Phys. Oceanogr.,* **32,** 353–375.

——, 2003: Kuroshio extension variability and forcing of the Pacific decadal oscillations: Responses and potential feedback. *J. Phys. Oceanogr.,* **33,** 2465–2482.

Stammer, D., 1997: Steric and wind-induced changes in TOPEX/Poseidon large-scale sea surface topography observations. *J. Geophys. Res.,* **102,** 20 987–21 009.

Stephens, C., J. I. Antonov, T. P. Boyer, M. E. Conkright, R. A. Locarnini, T. D. O'Brien, and H. E. Garcia, 2001: *Temperature*. Vol. 1, *World Ocean Atlas 2001,* NOAA Atlas NESDIS 49, 167 pp.

Sturges, W., and B. G. Hong, 1995: Wind forcing of the Atlantic thermocline along 32°N at low frequencies. *J. Phys. Oceanogr.,* **25,** 1706–1715.

Treguier, A.-M., and Coauthors, 2001: An eddy permitting model of the Atlantic circulation: Evaluating open boundary conditions. *J. Geophys. Res.,* **106,** 22 115–22 129.

Vega, A., Y. du-Penhoat, B. Dewitte, and O. Pizarro, 2003: Equatorial forcing of interannual Rossby waves in the eastern South Pacific. *Geophys. Res. Lett.,* **30,** 1197, doi:10.1029/2002GL015886.

Vivier, F., K. A. Kelly, and L. Thompson, 1999: Contributions of wind forcing, waves, and surface heating to sea surface height observations in the Pacific Ocean. *J. Geophys. Res.,* **104,** 20 767–20 788.